Journal of Materials Chemistry A

ROYAL SOCIETY OF CHEMISTRY

PAPER

View Article Online
View Journal | View Issue

Cite this: J. Mater. Chem. A, 2024, 12, 8769

Insights into the first multi-transition-metal containing Ruddlesden–Popper-type cathode for all-solid-state fluoride ion batteries†

Vanita Vanita, [a] Aamir Iqbal Waidha,[a] Sami Vasala,[b] Pascal Puphal,[d] Roland Schoch,[c] Pieter Glatzel,[b] Matthias Bauer[c] and Oliver Clemens *[a]

Promising cathode materials for fluoride-ion batteries (FIBs) are 3d transition metal containing oxides with Ruddlesden–Popper-type structure. So far, the multi-elemental compositions have not been investigated, but it could alternate the electrochemical performance similar to what has been found for cathode materials for lithium-ion batteries. In this study, we investigate RP type $La_2Ni_{0.75}Co_{0.25}O_{4.08}$ as an intercalation-based active cathode material for all-solid-state FIBs. We determine the structural changes of $La_2Ni_{0.75}Co_{0.25}O_{4.08}$ during fluoride intercalation/de-intercalation by *ex situ* X-ray diffraction, which showed that F^- insertion leads to transformation of the parent phase to three different phases. Changes in the Ni and Co oxidation states and coordination environment were examined by X-ray absorption spectroscopy and magnetic measurements in order to understand the complex reaction behaviour of the phases in detail, showing that the two transition metals behave differently in the charging and discharging process. Under optimized operating conditions, a cycle life of 120 cycles at a critical cut-off capacity of 40 mA h g^{-1} against Pb/PbF_2 was obtained, which is one of the highest observed for intercalation electrode materials in FIBs so far. The average coulombic efficiencies ranged from 85% to 90%. Thus, $La_2Ni_{0.75}Co_{0.25}O_{4.08}$ could be a promising candidate for cycling-stable high-energy cathode materials for all-solid-state FIBs.

Received 30th January 2024
Accepted 26th February 2024

DOI: 10.1039/d4ta00704b

rsc.li/materials-a

1 Introduction

Among the energy storage technologies, lithium-ion batteries (LIBs) have been the leading technology in terms of research and industrial application.[1] LIBs offer high energy density due to the high theoretical specific capacity of lithium (3860 mA h g^{-1}) and low density (0.534 g cm^{-3}) along with the lowest reduction potential (3.04 V *vs.* SHE). In addition numerous high voltage/high capacity cathodes, including Ni-rich transition metal oxides ($LiNi_{0.8}Co_{0.1}Mn_{0.1}O_2$, $LiNi_{0.8}Co_{0.15}Al_{0.05}O_2$, *etc.*), Li-rich ($Li_{1.2}Mn_{0.54}Ni_{0.13}Co_{0.13}O_2$) and high spinel ($LiMn_{1.5}Ni_{0.5}O_4$) electrode materials were developed but still some of them raise safety issues and show extreme capacity fading or have lower energy density.[2–6] In addition, LIBs suffer from critical issues like lithium dendrite growth leading to reduced safety due to the use of flammable organic electrolytes. Further, the limited availability of elemental resources such as Li can pose a supply risk in the future. Hence, it is important to investigate alternative energy storage technologies to keep up with the upcoming increased demand.

Fluoride ion batteries are interesting candidates for energy storage applications owing to the highest oxidation potential of the F^-/F_2 redox couple (+2.87 V *vs.* SHE) and thus the redox stability of the fluoride ion F^-, low atomic mass of F (18.998 g mol^{-1}) along with the abundance of fluorine itself.[7] FIBs have the potential to reach both superior gravimetric and volumetric energy density compared to LIBs, which is of interest for electric vehicles and other large-scale energy storage applications.[8] Hence, considering F^- as a stable ion for the charge transfer in the battery is a viable promising alternative.

The research on FIBs focused strongly on conversion-type cathode chemistries, *i.e.* metal/metal fluorides (Me/MeF_x)[9–15] which offer the highest theoretical capacities due to the possibility of taking part in a multi-electron conversion process. For example, Fichtner *et al.*[16] reported the use of CuF_2 as the conversion-type electrode material in FIBs. However, despite offering a high discharge capacity (360 mA h g^{-1}) in the first cycle, the consecutive cycles showed severe capacity fading. This

[a]Institute for Materials Science, University of Stuttgart, Materials Synthesis Group, Heisenbergstraße 3, 70569, Germany. E-mail: oliver.clemens@imw.uni-stuttgart.de; Fax: +49 711 685 51933

[b]ID26, European Synchrotron Radiation Facility (ESRF), 71 Avenue des Martyrs, 38000, Grenoble, France

[c]Institute of Inorganic Chemistry and Center for Sustainable Systems Design (CSSD), Paderborn University, Warburger Straße 100, 33098, Paderborn, Germany

[d]Max-Planck-Institute, Heisenbergstr. 1, 70569, Stuttgart, Germany

† Electronic supplementary information (ESI) available: Data supporting XRD, structural parameters, weight and atomic% from the EDAX analysis, XAS and EXAFS data, Fig. S1–S12 and Tables S1 and S2. See DOI: https://doi.org/10.1039/d4ta00704b

is related to large volume changes (~300%) upon cycling owing to the change in the crystal structure due to breaking and recombination of the chemical bonds, and these volume changes can lead to loss of contact between the active material, conductive carbon and the ion conductive electrode,[17–22] hence contributing to the loss of capacity over cycling.

To improve reversibility, intercalation-type cathodes can be viable alternatives. In these systems, the intercalation/deintercalation would result in a reduced degree of structural changes within the active material if the new bonds formed between fluoride and the elements of the host matrix are mainly of ionic nature. This requires the presence of redox-stable, soft cations, *e.g.*, alkaline earths or lanthanide cations within the structures. Few systems were studied and/or suggested.[10,17,23–26] Among them, Ruddlesden–Popper-type ((RP) $A_{n+1}B_nO_{3n+1}$, $n = 1$, 2) intercalation-based cathodes were found to be promising. Here, A is a rare earth or alkaline earth element and B is a transition metal ion. Within the crystal structure, an empty layer of interstitial anion sites is found between the perovskite and rock salt layer, which can be intercalated and deintercalated by the fluoride ions during the charging and discharging process.[27–29] Such cathodes are known to undergo significantly lower volume changes (~20%) compared to conversion-type cathodes (~50–200%), hence reducing contact loss between the active material, carbon additive and the ion conductive additive[30] on cycling. Previous investigations studied single transition metal-ion-containing RP compounds as cathodes. Amongst these La_2CoO_4,[23] La_2NiO_4,[24,26] $LaSrMnO_4$ (ref. [25] and [31]), and $Sr_2MnO_3F_2$ (ref. [31–33]) were studied intensively. $La_2NiO_{4.13}$ could be cycled for over 220 cycles with the coulombic efficiency between (95–99%) by limiting the critical cut-off capacity to 30 mA h g^{-1} compared to 60 cycles if the critical cut-off capacity was set to 50 mA h g^{-1} to limit detrimental side reactions of the carbon-based additive.[24]

To continue the further development of the RP-type intercalation-based cathodes in FIBs, it is of interest to investigate the role of multi-cation-containing RP cathodes. In the field of LIBs, it was observed that multi-transition metal ion-containing cathodes demonstrate improved rate capabilities and cyclability, *e.g.*, $LiMn_{1-x-y}Ni_xCo_yO_2$.[2–4,34] For such multi-cation compositions, a reduced degree of structural transformation (*e.g.*, layered to spinel) has been observed, and enhanced electron transport within the inorganic compound may play a further role in their beneficial activity in batteries. In this work, we report for the first time the battery characteristics of a multi-metal RP-type cathode material with composition $La_2Ni_{0.75}Co_{0.25}O_{4.08}$ which would have a theoretical capacity of 134 mA h g^{-1} for an uptake of two fluoride ions per formula unit. As a model system of choice and our previous results, La_2NiO_4 was chosen due to its excellent performance as the cathode candidate in FIBs and Co was chosen as the dopant, which has been a common dopant for nickelates in LIB chemistry as well. By combining different experimental techniques (X-ray diffraction, X-ray absorption spectroscopy, magnetic characterisation, and electron microscopy), we determine the individual redox characteristics of the different transition metal cations on battery cycling, showing that Ni and Co change their oxidation states at different states of charge.

2 Experimental

2.1 Material synthesis and electrochemical cell preparation

2.1.1 Preparation of the active cathode material $La_2Ni_{0.75}Co_{0.25}O_{4.08}$. The precursor $La_2Ni_{0.75}Co_{0.25}O_{4.08}$ was synthesized *via* a solid-state reaction. Stoichiometric ratios of La_2O_3 (Alfa Aesar, 99.9%, pre-dried at 1200 °C for 12 h before use), NiO (Sigma Aldrich, 99.99%, pre-dried at 700 °C for 12 h before use), and Co_3O_4 (Alfa Aesar, 99.99%) were ball milled in ZrO_2 jars for 1 h with the rotational speed of 600 rpm using a small amount of isopropanol as a dispersing agent. Then the mixture was heated at 1450 °C for 24 h under flowing argon (99.9%, 0.4 SLM (standard litre per minute) flow). The heating and cooling rates were 2 and 1 °C min^{-1} respectively.

2.1.2 Electrochemical cell components. All the cell components including electrolyte, anode, cathode materials and their respective composites were synthesized *via* ball milling using a ZrO_2 vial and balls (the vial was sealed inside an Ar-filled glovebox before the milling process) at individual rotation frequencies. To avoid an increase in temperature during milling, milling intervals of 10 min with 20 min of rest between each interval were chosen.

2.1.2.1 Solid electrolyte. $La_{0.9}Ba_{0.1}F_{2.9}$ (LaBF) was prepared by ball milling the stoichiometric amounts of LaF_3 (99.9%, Sigma Aldrich) and BaF_2 (99.9%, Sigma Aldrich) for 12 h at 600 rpm.

2.1.2.2 Anode composite. For the preparation of the Pb + PbF_2 anode composite, 45 wt% of elemental lead (Sigma-Aldrich, ≥99%), 45 wt% of PbF_2 (STREM chemicals, 99%) and 10 wt% of dried black carbon were milled at 600 rpm for 12 h. The anode system was chosen taking into account previously reported findings, which show this system to possess good kinetics of the conversion process due to the high ionic conductivity of PbF_2 and its low melting point.[35] This allows good referencing of novel materials with low overpotentials induced by the anode itself.

2.1.2.3 Cathode composite. For the preparation of the $La_2Ni_{0.75}Co_{0.25}O_{4.08}$ cathode composite, 30 wt% of as-synthesized $La_2Ni_{0.75}Co_{0.25}O_{4.08}$ was mixed with 60 wt% of $La_{0.9}Ba_{0.1}F_{2.9}$ and 10 wt% of dried carbon black to improve the ionic and electronic conductivity of the cathode material. The mixture was then ball milled for 3 h at a rotational speed of 250 rpm. The reduced rotation frequency is necessary to avoid amorphization and destruction of the layered structure.

2.2 Characterisation

2.2.1 Characterization of as-synthesized materials. XRD was used for analysing the composition of synthesized electrode composites and structural changes within the active material occurring during galvanostatic cycling at different states of charge. The measurements were recorded on a Rigaku Smart Lab diffractometer in Bragg–Brentano geometry with Cu K_α radiation and a Hypix-300 detector using the detector's X-ray

fluorescence reduction mode. All the samples were sealed inside an Ar-filled glovebox in low-background air-tight sample holders. Data were generally recorded in the angular range between $2\theta = 10°$ and 80° for a total measurement time of 4 h 18 min with a step size of 0.0050° and a divergence slit of 10 mm. The data were analysed using the Rietveld method with the programme TOPAS. The instrumental intensity distribution was determined using a reference scan of LaB_6. The microstructural parameters such as crystallite size and strain broadening were refined to adjust the peak shapes. To minimize quantification errors, thermal parameters were set to be identical for all atoms of all phases.

2.2.2 Electrochemical testing. Cells were prepared by pressing 200 mg of electrolyte, 5 mg of the cathode composite and 20 mg of the anode composite with a pressure of 2 t for 90 s using a pellet press inside an Ar-filled glovebox. The dimensions of the resulting pellet were approximately 1.3 mm in thickness and 7.3 mm in diameter. The pellets were spring-loaded into a modified air-tight Swagelok-type cell housing with the current collectors made of stainless steel shown in Fig. 1. All the electrochemical cells were loaded, sealed and prepared for further handling inside the glovebox. The sealed cells were cycled outside the glovebox at 170 °C and the Swagelok-type cell housing was covered with glass wool to minimize temperature fluctuations. Battery testing was performed using a Biologic VSP300 potentiostat with charging and discharging currents of +8.29 μA and −4.05 μA respectively, which translates to rates of C/15 and C/30 for charge and discharge respectively with respect to the theoretical capacity of the active cathode material (~134 mA h g^{-1} for conversion to $A_2BO_4F_2$). All the voltages are given as potential against the anode material. The mass of the active cathode material $La_2Ni_{0.75}Co_{0.25}O_{4.08}$ within the cell was ~1.5 mg, whereas the anode composite was used in large excess compared to the active cathode material, which helps to have the electrochemical curves being mainly dominated by the active cathode material. The discharge process was carried out directly after the charging process. Different cut-off capacities (such as 20/40/60/140 mA h g^{-1}) were tested.

2.2.3 X-ray absorption spectroscopy. For the pristine, cathode composite and fully charged samples, *ex situ* X-ray absorption spectroscopy (XAS) experiments at Ni and Co K-edges were carried out at DESY (Deutsches Elektronen-Synchrotron) beamline P65 in Hamburg, Germany. The measurements were performed at the third undulator harmonic using a Si-coated mirror to reject other harmonics, a maximum synchrotron ring current of 100 mA and a Si(111) double crystal monochromator in continuous mode (300 s per spectrum). The samples were prepared and handled under an inert atmosphere as BN-diluted pellets, sealed in Kapton® tape. Measurements on the Ni K-edge were carried out in transmission mode using a Ni-foil spectrum for energy calibration. Due to the lower Co concentration, the measurements were carried out in fluorescence geometry, whereby a Co foil spectrum was recorded before and after the measurements for energy calibration. For the $La_2Ni_{0.75}Co_{0.25}O_{4.08}$ samples charged at different cut-off charging/discharging capacities, *ex situ* high-energy-resolution fluorescence-detected X-ray absorption spectroscopy (HERFD-XAS) measurements at the Ni K-edge and the Co K-edge were carried out at beamline ID26 of the European Synchrotron Radiation Facility (ESRF) in Grenoble, France. For Co, the first undulator harmonic was used. For Ni, the third undulator harmonic was used. Higher harmonics were rejected by Si coated mirrors. When using the third harmonic, the first harmonic was removed using a diamond attenuator. The incident energy was selected and monochromatized by a Si(111) reflection from a double crystal monochromator in a continuous scan mode of 60–120 s per spectrum and synchrotron beam current of 75 mA. Ni foil was used for the calibration of the incident energy. Three Si(531) analyzer crystals were used to select the Co Kα emission and two Si(620) crystals for the Ni Kα emission. All crystals had a bending radius of 1 m and the emission was detected using an avalanche photodiode. The beam size was 0.1 × 0.2 mm^2 (vertical × horizontal) and the total flux was on the order of 5×10^{12} photons per second. The intensity was normalized to the incident flux. The pellets were sealed inside the Kapton® tape to minimize the air-exposure during the measurement. EXAFS analysis was done using an X-ray Larch.[36] Feff8 calculations for La_2NiO_4 were used to calculate paths for the fitting. Paths for equatorial and apical Ni–O and Ni–La were used in the fitting.

2.2.4 Scanning electron microscopy. Scanning electron microscopy was performed on a Zeiss EVO 15 SEM with an acceleration voltage of 15 kV. The samples were visualized using secondary electrons and backscattered electrons with an EDAX element detector. Elemental maps were obtained with a magnification of 826×, a resolution of 128.9 eV and a dwell time of 276.6 s. No additional coating was done on the samples due to the sufficient electronic conductivity of the electrodes.

2.2.5 Magnetic measurements. $La_2Ni_{0.75}Co_{0.25}O_{4.08}$ samples were scratched off from the cells and added to the gelatin capsules in mounted straw under an inert atmosphere between 6 and 10 mg and attached to the sample holder of a vibrating sample magnetometer for measuring the magnetization as a function of temperature and magnetic field in MPMS VSM SQUID, Quantum Design. The samples were examined in the DC mode in the temperature range of 300 K to 10 K at 1 T

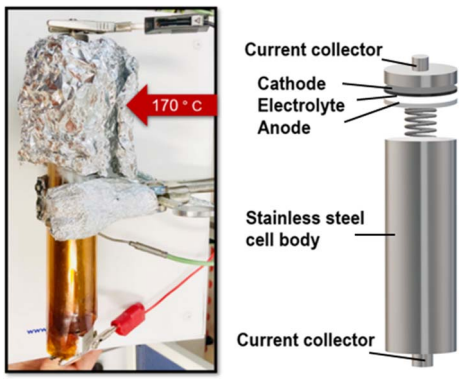

Fig. 1 Schematic of an operational electrochemical cell used for electrochemical measurements.

field. Field dependent measurements were recorded at 10 K in the range between −7 and 7 T.

3 Results and discussion

3.1 Structure and morphology of $La_2Ni_{0.75}Co_{0.25}O_{4.08}$ and its cathode composite

$La_2Ni_{0.75}Co_{0.25}O_{4.08}$ (oxygen content determined *via* iodometric titration) was obtained as a phase-pure material (see Fig. 2). The lattice parameters were found to be $a = 3.88125(4)$ Å, $c = 12.57064(18)$ Å, $V_{f.u.} = 189.365(4)$ Å^3, and the unit cell volume is comparable to that of La_2NiO_4 (189.05 Å^3), which is expected from the similar radii of the different transition metals (if Co and Ni ions are trivalent with very similar ionic radius $r_{Co^{2+}} = 0.65$ Å, $r_{Co^{3+}} = 0.545$ Å and $r_{Ni^{2+}} = 0.69$ Å, $r_{Ni^{3+}} = 0.56$ Å, both low spin).

The SEM micrograph of the as-synthesized compound is given in Fig. 3. The as-synthesized particles show a coarse well-sintered structure which can be attributed to the high sintering temperatures used for the synthesis of the parent RP compound (the educt mixture after ball milling consists of more loose particles (see Fig. S11†)). Elemental mapping (see Fig. 3c) shows the homogenous uniform distribution of the constituent elements La, Ni and Co within the as-synthesized parent RP oxide. Further, the weight fractions of the constituent elements in $La_2Ni_{0.75}Co_{0.25}O_{4.08}$ observed from EDAX analysis (shown in Table S2†) are in agreement with their initially weighed proportions within the precursor mixture.

In order to be used as the cathode in the all-solid-state FIB, the as-synthesized $La_2Ni_{0.75}Co_{0.25}O_{4.08}$ was ball-milled together with the electronically conductive carbon matrix along with ionically conductive $La_{0.9}Ba_{0.1}F_{2.9}$ solid electrolyte. This serves not only to mix all the components together to form an intimate interfacial contact but also to reduce the particle size of the active material and to increase the electrochemically active surface area of the active material for the redox reactions. For the successful operation of the fabricated all-solid-state FIB, elevated operation temperatures of around 170 °C are necessary in order to achieve sufficient fluoride ion conductivity of the $La_{0.9}Ba_{0.1}F_{2.9}$ solid electrolyte, which is reported to be in the order of 10^{-4} S cm^{-1}.[17] The temperature stability of the cathode composite mixture was also investigated by heating it at 170 °C for 100 h, *i.e.*, conditions similar to the operating conditions of the FIB. From the comparison of the lattice parameters obtained from the Rietveld fits of the X-ray diffractograms of the as-synthesized parent oxide, ball-milled cathode, composite and heat-treated cathode composite, it is confirmed that ball milling and heating the composite do not influence the nature of the cathode active material and that any structural changes induced are strictly from the electrochemical reaction (see Fig. 2b and Table S1 of the ESI†). Further, the weight fractions of $La_2Ni_{0.75}Co_{0.25}O_{4.08}$ and the solid electrolyte within the cathode composite determined from Rietveld analysis of the XRD data match well with the expected values.

To test the electrochemical performance of $La_2Ni_{0.75}Co_{0.25}O_{4.08}$ as a cathode in FIBs, galvanostatic charging and discharging curves were recorded in an all-solid-state battery comprising $La_2Ni_{0.75}Co_{0.25}O_{4.08}$ II $La_{0.9}Ba_{0.1}F_{2.9}$ II Pb–PbF_2 within the modified stainless-steel Swagelok-type cell at 170 °C as shown in Fig. 1. First, the structural changes induced upon F^- intercalation were determined. For this, separate cells were galvanostatically charged to different capacities up to 600 mA h g^{-1} (which is far beyond the theoretical capacity of the active cathode material and can thus help to indicate potential and capacity ranges in which side reactions of the carbon-based additive can occur) and analyzed by *ex situ* X-ray diffraction measurements of the cathode side of the pellet (see Fig. 4). Overall, the charging curve can be divided into three different zones as indicated in Fig. 4a.

(1) A sharp increase in the voltage from 0.2 V to 0.45 V *vs.* Pb/PbF_2 is observed. Such a sharp increase corresponds well with the initiation of the electrochemical reaction involving different processes like F^- ion transport from the anode towards the cathode, *i.e.*, the mass transport along with the accumulation of the charge at the electrolyte/cathode interface. In this region, the capacity contribution taken up is very low (~2 mA h g^{-1}).

The potential change from 0.45 to 0.55 V proceeds over a capacity range of 20–30 mA h g^{-1}. This corresponds to the first oxidation of the transition metal-ions of the RP-type compound from fluoride-ion incorporation. The process only induces moderate changes of the lattice parameters (see later in this section), and is accompanied by broadening and asymmetry of

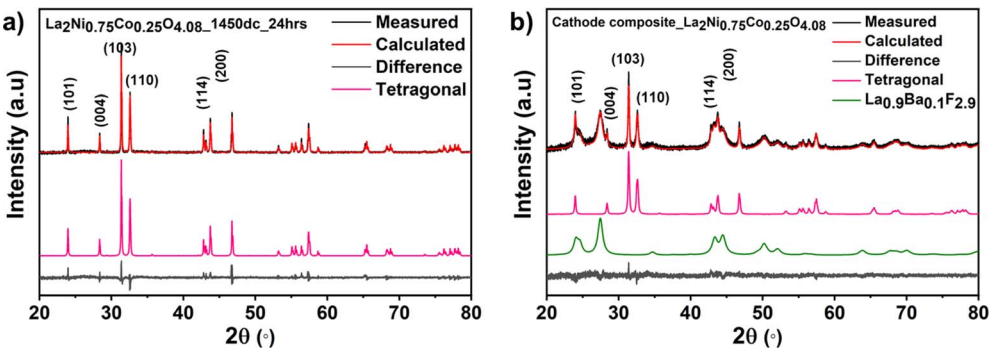

Fig. 2 Rietveld fit of the (a) X-ray diffraction pattern of $La_2Ni_{0.75}Co_{0.25}O_{4.08}$. The Miller indices of main reflections belonging to the active material are marked. (b) Cathode composite of $La_2Ni_{0.75}Co_{0.25}O_{4.08}$ containing additional reflections of the electrolyte $La_{0.9}Ba_{0.1}F_{2.9}$.

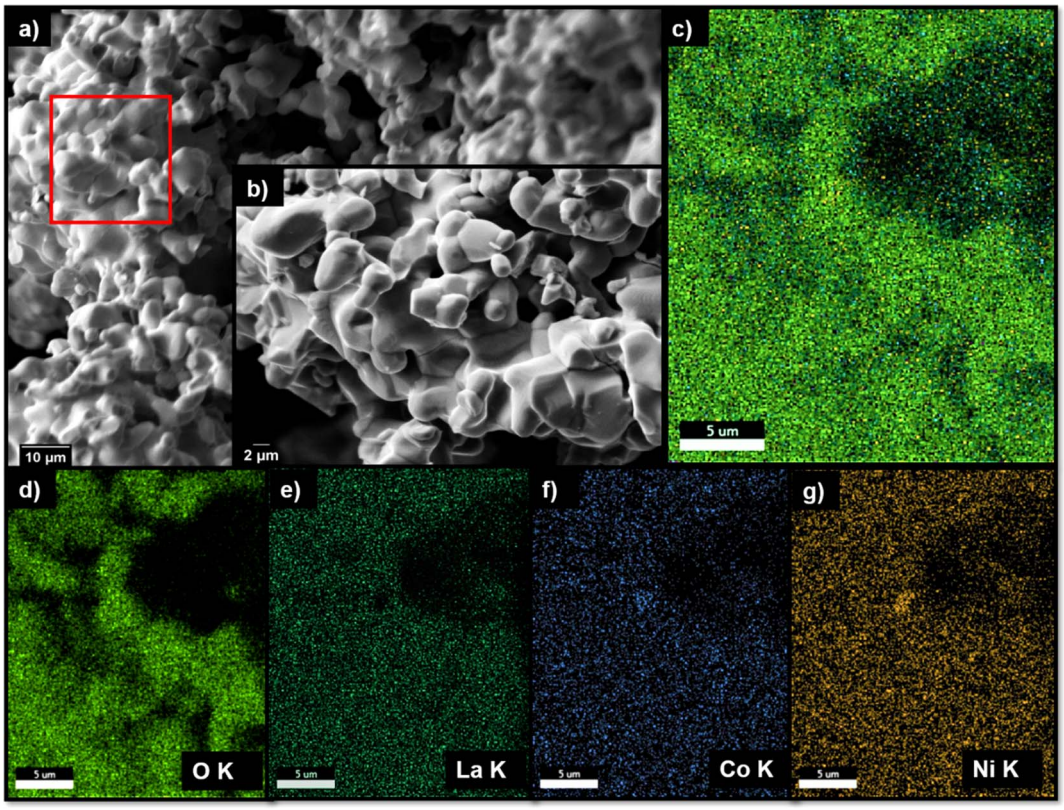

Fig. 3 SEM micrograph of $La_2Ni_{0.75}Co_{0.25}O_{4.08}$ at (a) low magnification (800×), (b) higher magnification (6000×), elemental mapping of a specific area (red marked) (c) overlapped elements and (d–g) individual elements.

the reflections (in particular those with $l \neq 0$, *e.g.*, shoulders appearing on the (103) reflection), see Fig. 4d. This likely originates from the lattice distortions occurring on inserting F^- in the interstitial anion sites,[25] and inhomogeneous F^- distribution in the active material particles.

(2) Two processes likely occur simultaneously in the long plateau at ~1.2–1.3 V, which are the fluorination of the carbon black additive in addition to the formation of a high fluorine content RP-type phase with a lattice parameter *c* around 15.275(3) Å, which has also been found for related materials[37,38] and is indicated by an additional reflection at 29° within the X-ray diffractograms (Fig. 4e). As the charging process within this plateau proceeds, the reflection at 29° increases in intensity along with the decrease in the intensity of the indicative reflections of the parent (-related) compound $La_2Ni_{0.75}Co_{0.25}O_{4.08}$ at ~31.5° and ~32.5° respectively. At the end of this plateau, a full transformation of the RP-type phase to the phase with large lattice parameter *c* can be observed, and the reflections belonging to this phase become sharper again, indicating that defect-related strain broadening is reduced from the increased fluorination. We would like to emphasize here that pure carbon does only show a very short plateau at 1.2 V (see Fig. S12†); the active RP-type material has a redox-catalytic activity for oxidatively fluorinating the carbon, as described previously by Nowroozi.[24,25]

(3) Another potential increase beyond a specific capacity of 600 mA h g^{-1} cannot be assigned to further reaction of the RP-type phase, and likely corresponds to further degradation/oxidation of the carbon matrix,[23–25,37,39,40] see also Fig. S12.†

Rietveld analysis can be used to analyze the details of the structural changes occurring on charging RP-type phases in FIBs. From this analysis, weight fractions as well as lattice parameters of the individual phases can be extracted. The results of this analysis (performed on the patterns shown in Fig. 5) can provide a more detailed understanding of the charging process. From a close inspection of the shape of the reflections of the RP-type phases, it becomes clear that it is not possible to refine the pattern of the low-fluorine content phases with a single RP-type phase, and multiple RP-type phases were found to be required to obtain an acceptable fit of the diffraction pattern (see Fig. S2†). On increased charging, we find changes in the different modifications of RP-type phases present along with changes in their phase fractions (see Fig. 6a). Partly, the lattice parameters and cell volumes of the individual phases can be slightly affected depending on the detailed state of charge.

After heating, the sample is mainly composed of an orthorhombic phase (see Section 3.1), which we assign the label orthorhombic #1 in the following discussion. Orthorhombic distortions within RP-type material can have different origins: pure La_2NiO_4 is known to crystallize in the orthorhombic space group *Pmnb*, where the distortion originates from tilting of the octahedra within the *a*/*b*-plane, which mainly changes the coordination around the La-ions. In addition, orthorhombic

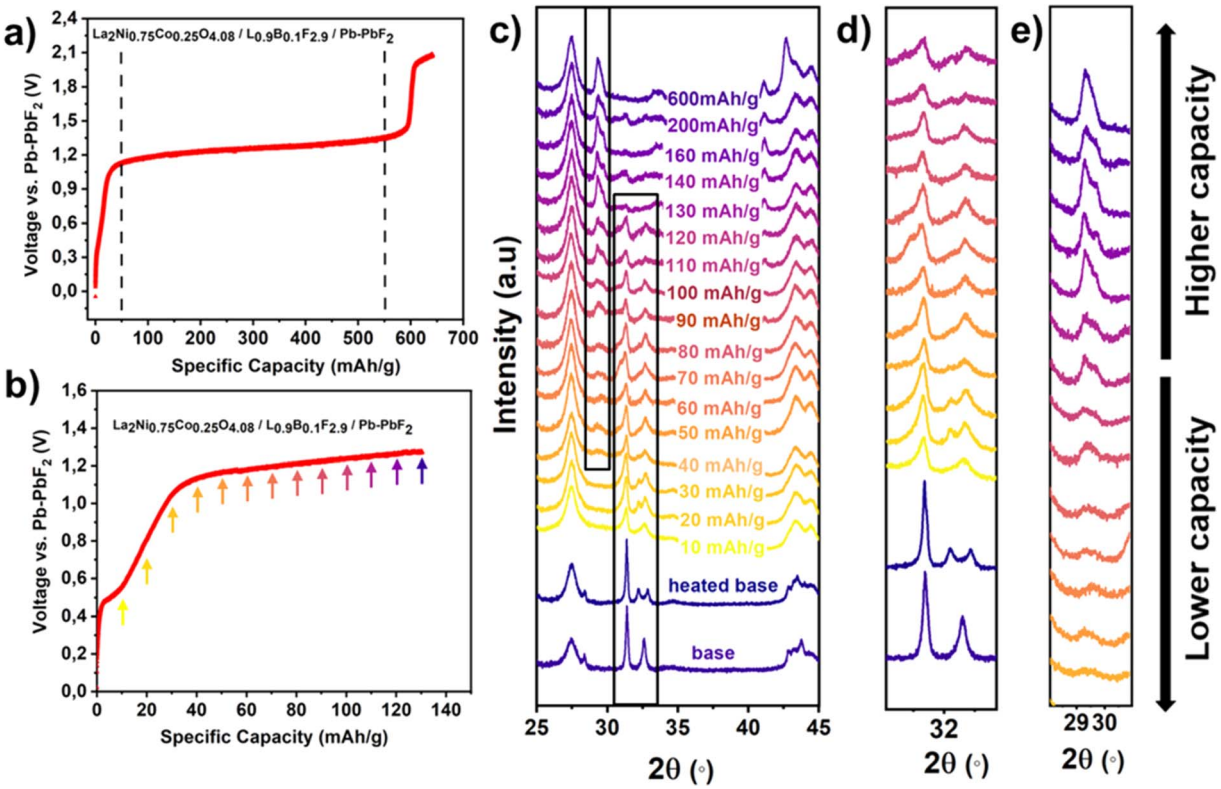

Fig. 4 (a) Typical charging curve for the $La_2Ni_{0.75}Co_{0.25}O_{4.08}$/$La_{0.9}Ba_{0.1}F_{2.9}$/Pb–$PbF_2$ cell. (b) Below shows the details of the lower capacity range and the coloured arrows mark the chosen cut-off capacities for the charging process where the *ex situ* XRD measurements were taken, (c) *ex situ* diffraction pattern obtained from the individual cells charged at the different cut-off capacities, (d) enlarged view of the peak at 32° and (e) enlarged view of the peak at 29.5°. Full refinement of the single pattern with partial fit curves for different phases is shown in the ESI.†

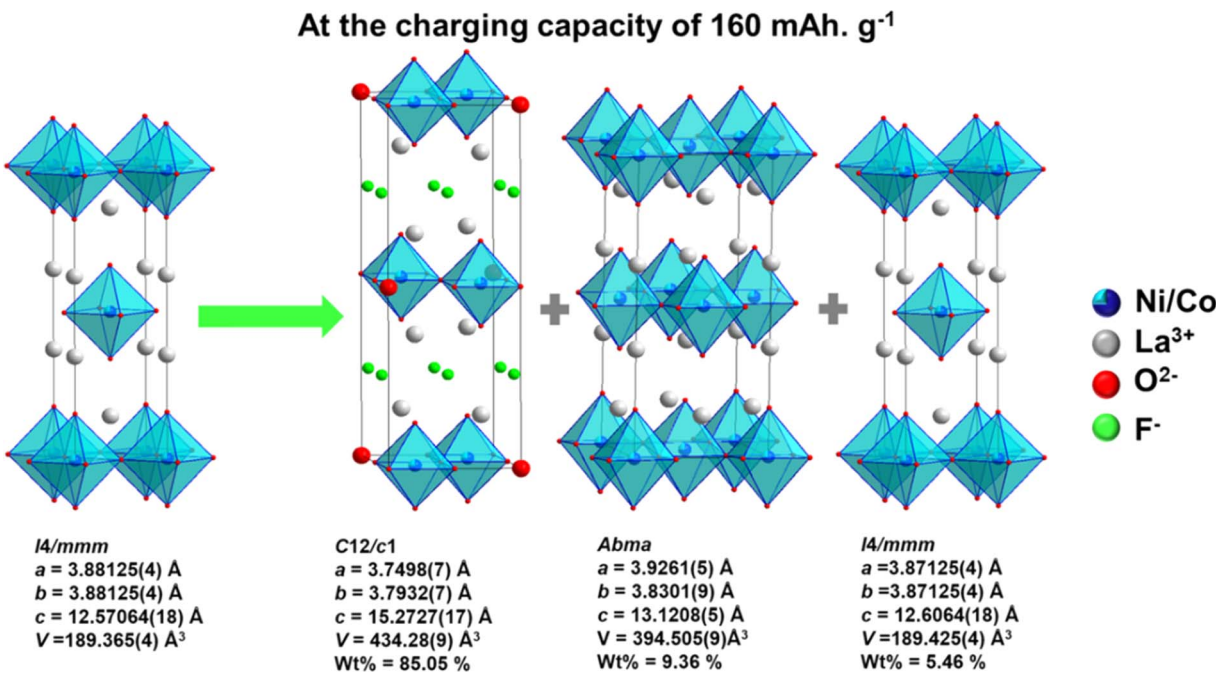

Fig. 5 Scheme of structural changes in $La_2Ni_{0.75}Co_{0.25}O_{4.08}$ – the schematic illustrates the non-fluorinated $La_2Ni_{0.75}Co_{0.25}O_{4.08}$ (left) and the fluorinated phase along with two other different phases (right).

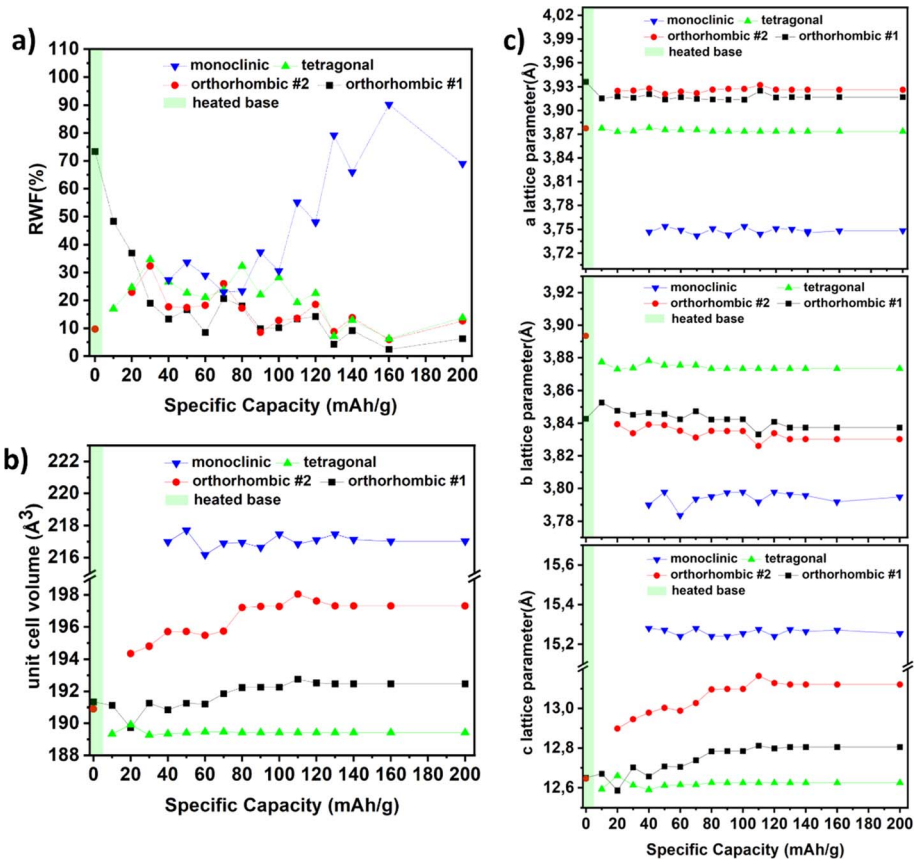

Fig. 6 (a) Relative weight fractions (RWFs) of the phases formed. (b) Volume changes of different phases formed on charging up to various cut-off capacities. (c) Lattice parameters of different phases formed on charging up to various cut-off capacities.

distortions can also occur when filling of the interstitial sites takes place, *e.g.*, as observed for $La_2NiO_3F_2$ with space group *Cccm*, in which case the orthorhombic distortion is caused by the additional space required by the fluoride ions within the interlayers and accompanied by a moderate increase of the lattice parameter *c* (see Fig. 6c). Both, tilting occurring on either the increased ordering of anions or on small degrees of anion exchange reactions according to the following reaction equation, are possible and the individual effects cannot be separated precisely:

$$A_2BO_4 + 2xF^- \rightarrow A_2BO_{4-x}F_{2x}$$

Upon charging beyond 10 mA h g^{-1} in the first region, the orthorhombic #1 phase fraction is found to decrease significantly. In addition, a tetragonal phase, as well as another orthorhombic phase (labeled as orthorhombic #2) appears. The tetragonal phase possesses cell parameters which appear to be fairly independent of the state of charge, in contrast to what is found for the orthorhombic #1 and #2 phases. The orthorhombic #2 and the tetragonal phase show an increase in the *c*-axis; in addition, the orthorhombic #2 phase shows an increase in the splitting of the *a*/*b*-lattice parameters at an overall increased cell volume as compared to the original state after heating. These changes remind us about the structural distortions found for orthorhombic $La_2NiO_3F_2$,[41,42] and we interpret this structural behavior as being induced by the fluoride-ions accumulating within the interstitial layers at a low content and inducing an orthorhombic distortion to be accommodated therein. The maximum overall amount of the orthorhombic phases is found between 30 and 40 mA h g^{-1}, for which these phases amount to approximately 50% of the total RP-type phases. Considering that carbon side reactions mainly occur above 1.2 V and not in this potential range, one can estimate that the orthorhombic phases contain a maximum of 1 F per formula unit, further supported by the absence of a large increase of the *c*-axis, *i.e.* possess a maximum composition of $La_2Ni_{0.75}Co_{0.25}O_{4.08}F_1$.

Upon further charging to a higher cut-off capacity, *i.e.* up to 160 mA h g^{-1}, an additional phase can be observed in the X-ray diffractograms (Fig. 4e) with an indicative reflection at 29°. Schematic illustrations of fluorinated and non-fluorinated $La_2Ni_{0.75}Co_{0.25}O_{4.08}$ state have been shown in Fig. 5. From the Rietveld refinements, it was found that this phase can be refined within a monoclinic RP-type phase (the crystal system is indicated from the splitting of the reflections), for which we took the structural model with symmetry *C*2/*c* as previously observed for $La_2NiO_4F_{1.7}$ from electron diffraction.[30] The relative weight fraction (Fig. 6a) of this phase was found to increase

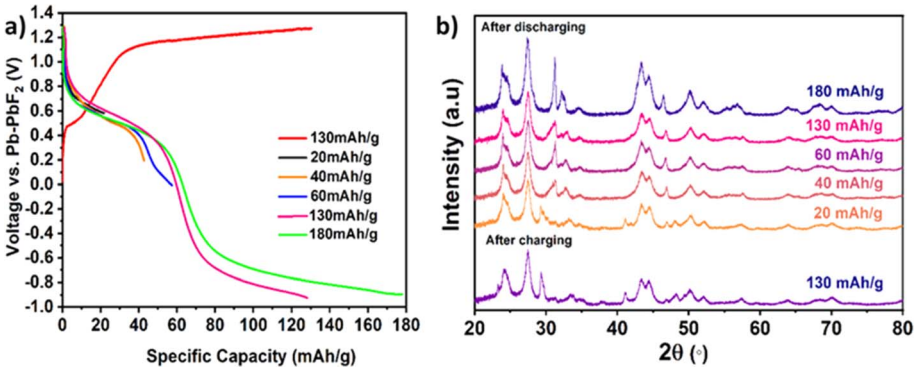

Fig. 7 (a) Discharge curves for cells charged to a capacity of 130 mA h g^{-1} and discharged up to various cut-off capacities. (b) Diffraction patterns for the individual cells discharged to different discharge capacities.

with increased charging between 40 mA h g^{-1} to 160 mA h g^{-1}. As can be seen from Fig. 6b, this monoclinic phase has an increased volume per $La_2Ni_{0.75}Co_{0.25}O_{4.08}$ unit by about ~28 $Å^3$ compared to the tetragonal, orthorhombic #1 and orthorhombic #2 phases. This volume change is indicative of a highly fluorinated phase with all interstitial sites occupied by fluoride ions[17,24–26,41,43] and mainly originates from the large increase of the *c*-axis length to ~15.275(3) Å, whereas the *a*/*b* parameters contract due to shortened (Co/Ni)–O bonds from the oxidation process (Fig. 6c). The chemical formula for this phase is likely close to $La_2Ni_{0.75}Co_{0.25}O_{4.08}F_{1.92-\delta}$ (see also XAS analysis reported in Section 3.3). We note that on charging, a change of the relative weight fraction of the monoclinic phase occurs, whereas its unit cell volume remains mainly constant (Fig. 6b). This can be interpreted in the sense that this phase is saturated with fluoride ions already once it starts to occur, and might have a narrow compositional flexibility. The structural changes on fluorination are also in accordance with what has been observed for the chemical fluorination of $Sr_2TiO_3F_2$ (c = 15.89 Å) and $La_2CoO_{4+d}F_y$ (c = 15.1930(6)) and electrochemical fluorinations of $La_2CoO_4F_y$ (c = 15.292(1) Å), $La_2NiO_{4.13}F_y$ (c = 15.255(30) Å), and $LaSrMnO_4F_{2-x}$ (c = 15.631(7) Å).[10,23–25,41]

In order to understand the electrochemical defluorination behavior of the parent RP-type phases, the parent oxide was first charged to 130 mA h g^{-1} followed by discharging to different discharge capacities (20, 40, 60, 130 and 180 mA h g^{-1}), shown in Fig. 7a and subsequent *ex situ* XRD analysis (see Fig. 7b). For the sample discharged to 20 mA h g^{-1}, it is found that the monoclinic phase is still the major phase present along with the relatively lower weight fractions of the tetragonal, orthorhombic #1 and orthorhombic #2 phases. The major indicative reflection of the monoclinic phase at 29° is still visible for the discharged state of 20 mA h g^{-1} (see Fig. 7b), and no significant changes are observed for the lattice parameters. Upon discharging to 40 mA h g^{-1}, the indicative reflection of the monoclinic phase is no longer visible and only the tetragonal and two orthorhombic modifications are found. For high coulombic efficiency (an absence of side reactions on charging), the discharge capacity of 40 mA h g^{-1} would correspond to the charging capacity of 90 mA h g^{-1}. Interestingly, there is a clear difference between the relative weight fractions of the different phases at this stage shown in Fig. 8a. For charging to 90 mA h g^{-1}, the main phase was found to be the monoclinic phase along with relatively lower weight fractions of the other phases; however, for reaching a comparable state on discharging, the monoclinic phase is completely absent. This also suggests the possible overlapping of side reactions along with the charging of the parent RP oxide phase. Such side reactions can be attributed to carbon fluorination which is well known in FIBs.[24,26,37,44,45]

Compared to charged cells, the discharged cells show similar lattice characteristics for the orthorhombic phase #1 (a ~ 3.9287 Å, b ~ 3.8463 Å, c ~ 12.8049 Å), orthorhombic phase #2 (a ~ 3.9411 Å, b ~ 3.8322 Å, c ~ 13.0832 Å) and tetragonal phase (a ~ 3.8733 Å, b ~ 3.8733 Å, c ~ 12.6272 Å) as seen in Fig. 8. Discharging to high discharge capacities (130/180 mA h g^{-1}), *i.e.*, inducing a larger reduction on discharging than oxidation on the prior charging, resulted in negative potentials against Pb/PbF_2, with a decrease of the lattice parameters a, b and a decrease in lattice parameter c, resulting in a lower unit cell volume for both the orthorhombic phases. The lattice parameters of the discharged phases are similar to that of the charged phase without a strong indication of amorphisation from the refined weight fractions, hence confirming structurally reversible fluorination/defluorination under maintenance of the principle structural arrangement.

3.2 Cycling stability of $La_2Ni_{0.75}Co_{0.25}O_{4.08}$ as the cathode in FIBs

For its application in the FIBs as a potential cathode material, an attempt was made to determine the cycling stability of the parent RP phase. To do so, we examined cell reversibility on charging and discharging the cell to cutoff conditions of either 40 mA h g^{-1} or potentials of 1.3 V and 0 V against Pb/PbF_2 on charging/discharging respectively. The capacity conditions were chosen according to the findings reported in Section 3.1, which show an increased amount of side reactions, if charging proceeds above 40 mA h g^{-1}. As seen from Fig. 9, it is observed that the discharge capacity increases within the first 6 cycles after charging to the cutoff capacity of 40 mA h g^{-1}. This enhanced discharge capacity as a function of cycle number can be related to reduced side reactions of the carbon additives on increased cycling.[46,47] Thus, an increase in cycle number leads to

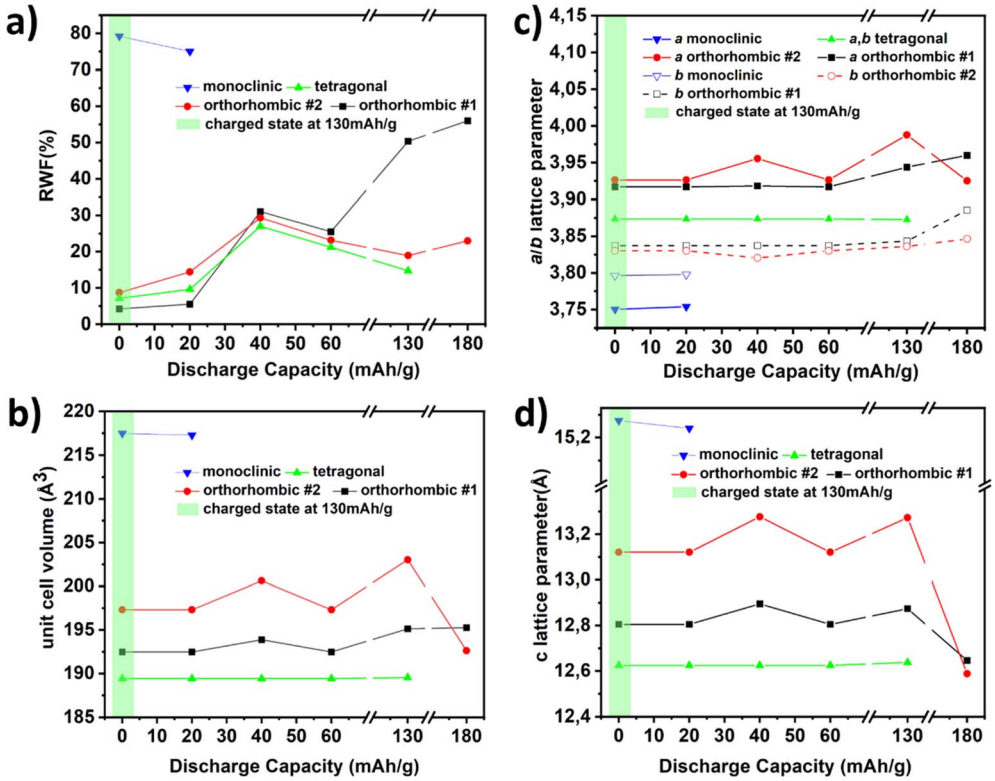

Fig. 8 (a) RWFs of the phases formed (b) volume changes (c) lattice constants *a*, *b* and (d) lattice constant *c* of different phases formed on discharging up to various cut-off capacities.

higher active material utilization *i.e.* intercalation of F^- within the RP phase as opposed to the side reactions, thus leading to higher discharge capacities. In previous studies, La_2NiO_4 was cycled at the cut-off capacity of 30 mA h g^{-1}, whereas $La_2Ni_{0.75}Co_{0.25}O_{4.08}$ has shown certain stability at the increased cut-off capacity of 40 mA h g^{-1} and shows the cycling stability up to 120 cycles. Already after the first cycle (see Fig. 9a), the charging plateau shifted from lower potential to high potential by about 0.3 V and the specific capacity increased by ~11%. After the second cycle, the charging plateau shifted again by ~+0.2 V together with a further increase of the specific capacity of 32%. These voltage gaps are in agreement with the low coulombic efficiencies within the first cycles originating from the presence of side reactions such as decomposition of the carbon matrix, as discussed before. After this, the curves only show minor changes regarding their general shape up to 120 cycles (apart from a continuous increase of discharge capacity by 0.2–0.3 mA h per g per cycle, see Fig. S3,† resulting in improved coulombic efficiency). The discharge capacity remains highly stable with the coulombic efficiency of around 90% without significant capacity fading for 120 cycles as shown in Fig. 9b. La_2NiO_4 reported previously was found to show higher coulombic efficiencies between 95 and 99%.[24] The lower coulombic efficiency of $La_2Ni_{0.75}Co_{0.25}O_{4.08}$ of up to 90% is thus likely related to consumptive processes at low cycles, and Co seems to be the most plausible origin for introducing the side reactions in the carbon additive. However, the capacity retention is also superior in comparison to pure La_2CoO_4.[23] In contrast to this, Co can also have beneficial influences on the cycling behavior. This was observed when cycling the material close to the theoretical cut-off capacity of 130 mA h g^{-1}.

Under these conditions, a discharge capacity as high as 80 mA h g^{-1} could be observed after the 5th cycle, which is increased compared to pure La_2NiO_4 under such conditions (compare Fig. 9c to d).

The structural changes of the RP-type compounds at higher cycle numbers were examined within the first 21 charge–discharge cycles for the cut-off capacity of 40 mA h g^{-1} by stopping at the discharged state as shown in Fig. 10. *Ex situ* XRD measurements were done on the cathode composition and Fig. 10 shows the RWFs of the phases present in the cycled cells. The XRD patterns of the RP-type phases can be well fitted with the tetragonal phase and two orthorhombic phases. Compared to charged and discharged states, the cells cycled for 21 cycles show similar values of lattice parameters than the discharged state for orthorhombic phase #1 ($a \sim 3.9550$ Å, $b \sim 3.8290$ Å, $c \sim 12.988(4)$ Å). For orthorhombic phase #2, *a* lattice parameter seems to increase slightly and the lattice parameters *b* and *c* stay similar. For the tetragonal phase, the most significant change is observed in the 21st cycle, at which it seems to have a higher *c* lattice parameter together with an increased cell volume. These findings indicate that the reduced coulombic efficiency could also be partly related to changes in the structure and composition in the discharged state. This could be possibly explained by a redistribution of fluoride and oxide ions within the different fractions of RP-type phases formed on cycling. For

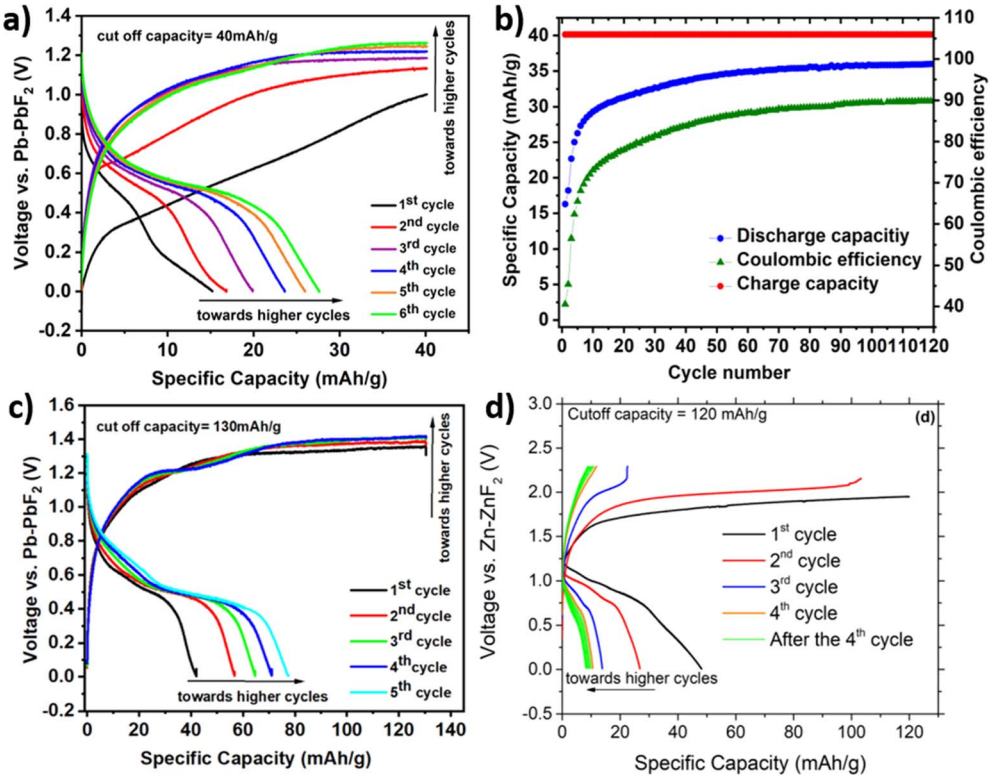

Fig. 9 Cycling curves of $La_2Ni_{0.75}Co_{0.25}O_{4.08}$/Pb–$PbF_2$ at $T = 170$ °C, $I_{charge} = +8.0294$ μA, $I_{discharge} = -4.0145$ μA, at the charging capacities (a) 40 mA h g^{-1} and (c) 130 mA h g^{-1},(b) charge/discharge capacities and coulombic efficiency against cycle number for the cells with the cut-off capacities of 40 mA h g^{-1} and (d) cycling curves of $La_2NiO_{4.13}$ under the charging condition of 120 mA h g^{-1}. Reproduced with permission.[1] Copyright 2023, *Commun. Mater.*, 2020, 1.

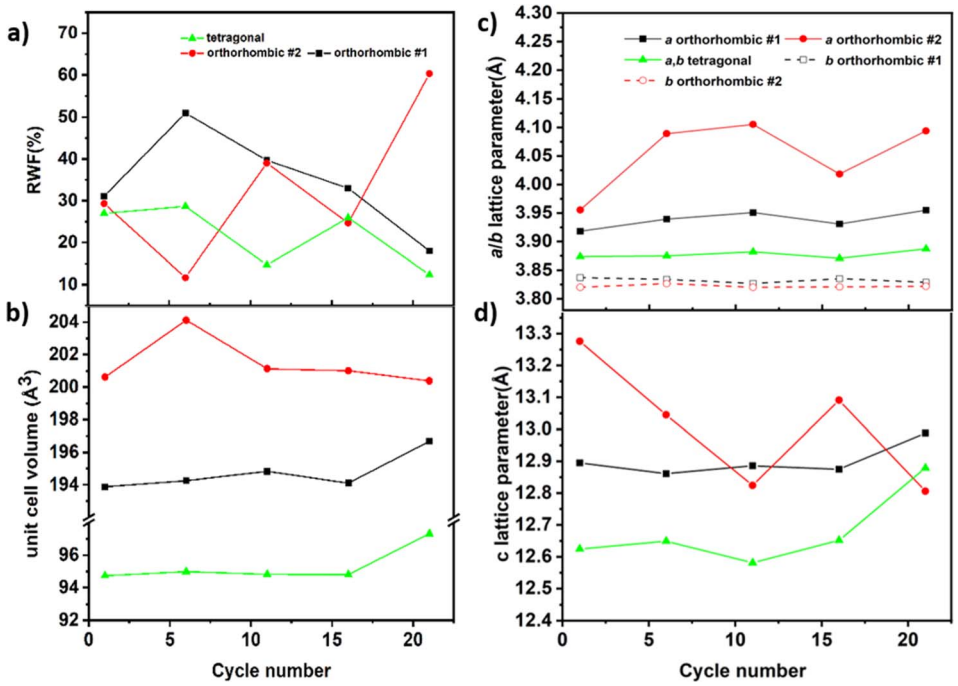

Fig. 10 (a) RWFs of the phases present in the cells operated for different cycle numbers and stopped in the discharge state, (b) volume changes and (c) lattice constants of different phases formed on charging–discharging of the cell at different number of cycles.

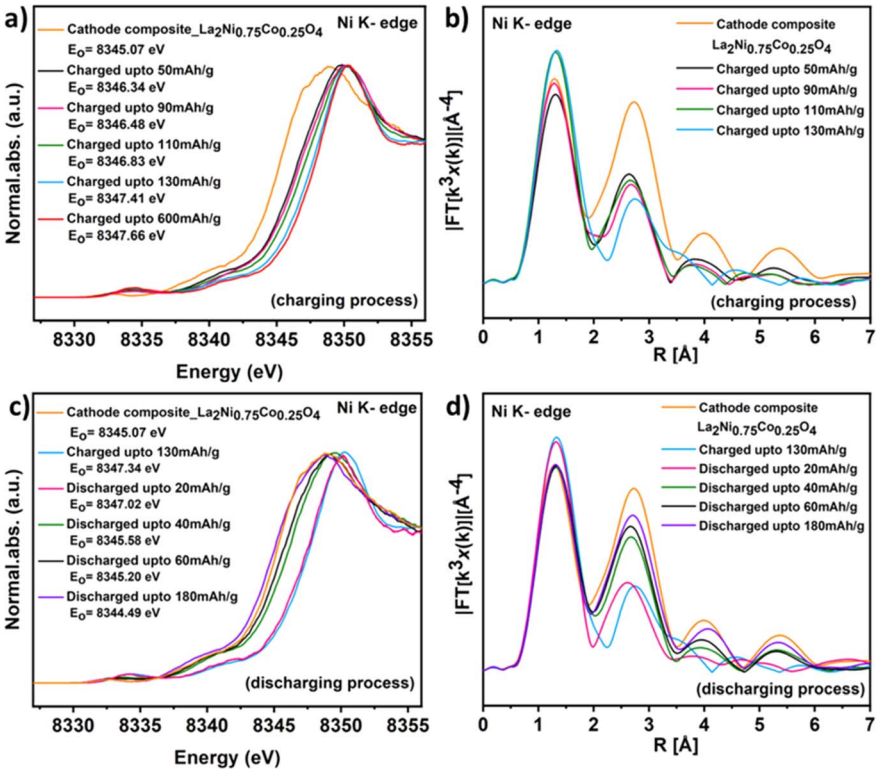

Fig. 11 HERFD-XAS at the Ni K-edge (a) XANES of $La_2Ni_{0.75}Co_{0.25}O_{4.08}$ after F^- insertion, (b) EXAFS of $La_2Ni_{0.75}Co_{0.25}O_{4.08}$ after F^- insertion, (c) XANES of $La_2Ni_{0.75}Co_{0.25}O_{4.08}$ after F^- extraction and (d) EXAFS of $La_2Ni_{0.75}Co_{0.25}O_{4.08}$ after F^- extraction.

example, if one phase enriches in oxygen and the other in fluorine, the oxygen-rich phase would not be accessible for further fluoride extraction to the same extent.

3.3 Influence of charging/discharging on the electronic states and local structure of Ni and Co ions

Diffraction measurements, though important to characterize the overall structural changes on charging and discharging, are unsuitable to discriminate the individual behavior of the transition metals in multi-metal compounds. Thus, element specific X-ray absorption spectra were recorded to determine changes in the oxidation states as well as individual structural changes around the Ni and Co cations. First, we note that the mixing of the RP-type compound together with carbon and $La_{0.9}Ba_{0.1}F_{2.9}$ has no influence on the position of the edges, and only the charging influences the position of the Ni and Co edges significantly, see Fig. S4.† However, clear changes in the absorption edges could be determined for the cells charged/discharged to different cut-off capacities. The Ni edge (see Fig. 11a) behaves similarly to what has been observed for pure $La_2NiO_{4+\delta}$.[24] On charging, the Ni edge shifts progressively to higher energies on increased fluoride uptake of the cathode side. The same trend was also observed for the pre edges of Ni shown in Fig. S5.† The pre-edge is more sensitive to the oxidation state, whereas the main edge has strong contribution from the bond lengths and the type of coordinating anions. The similar behavior of both the absorption energies gives strong confirmation that the Ni oxidation state does change and not just the structure around the atoms. Overall, a change of the oxidation state close to tetravalent Ni^{4+} is indicated when charging the cell to the highest state of charge.[48] This is also in agreement with the changes of the bond distances around the Ni cation (see Table 1), which can be derived from the EXAFS region of the spectra (see Fig. 11b); here, we would like to emphasize that the errors of the bond distances are high and these values should only be interpreted as a general trend. The apical bond distances increase by about 25 pm, whereas the equatorial bonds contract by about 5 pm; the equatorial trend is well supported by the refinement of lattice parameters, which mainly influence them. On discharging the compound to

Table 1 Ni–O bond distances of $La_2Ni_{0.75}Co_{0.25}O_{4.08}$ under different charging conditions. Errors are in the order of ±0.02–0.05 for the equatorial (eq.) and of ±0.04–0.10 for the apical (ap.) bond distances

Sample	Ni–O eq. bond (pm)	Ni–O ap. bond (pm)
Cathode composite	194	227
Charged up to 50 mA h g^{-1}	190	248
Charged up to 90 mA h g^{-1}	188	254
Charged up to 110 mA h g^{-1}	188	245
Charged up to 130 mA h g^{-1}	188	250
Discharged up to 20 mA h g^{-1}	188	246
Discharged up to 40 mA h g^{-1}	193	249
Discharged up to 60 mA h g^{-1}	194	238
Discharged up to 180 mA h g^{-1}	194	228

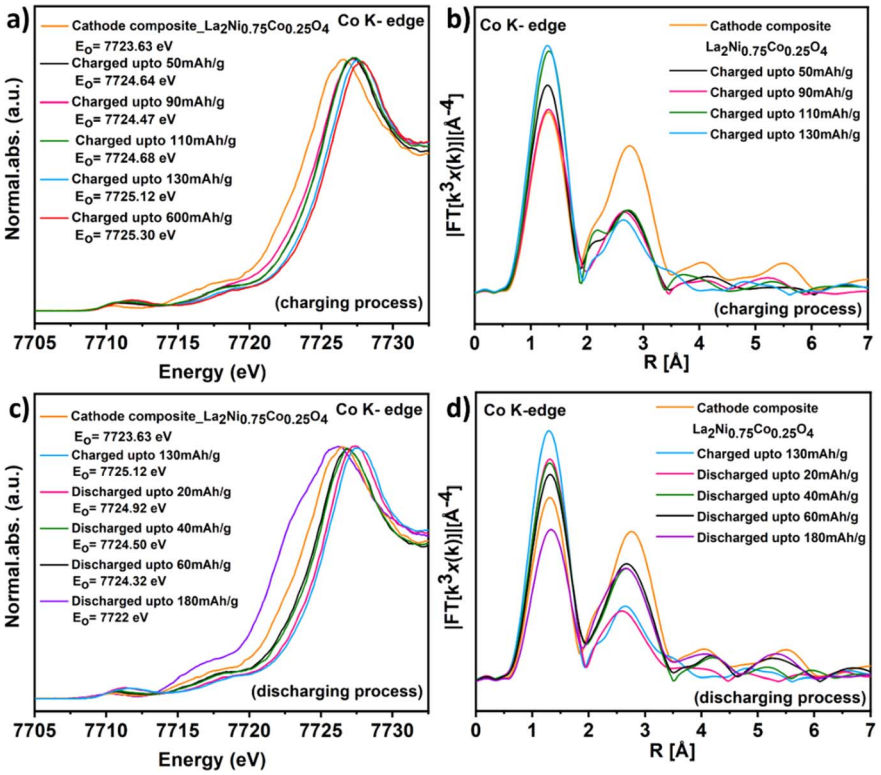

Fig. 12 HERFD-XAS at the Co K-edge (a) XANES of $La_2Ni_{0.75}Co_{0.25}O_{4.08}$ after F^- insertion, (b) EXAFS of $La_2Ni_{0.75}Co_{0.25}O_{4.08}$ after F^- insertion, (c) XANES of $La_2Ni_{0.75}Co_{0.25}O_{4.08}$ after F^- extraction and (d) EXAFS of $La_2Ni_{0.75}Co_{0.25}O_{4.08}$ after F^- extraction.

negative potentials, this process seems to be well reversible. The edge position of Ni shifts back close to the original position of the sample before charging, and the bond distances are similar to the sample before charging (see Fig. 11c, d and Table 1). However, we note that the apical anion only moves back to the original position at high discharge capacities.

For Co, interesting differences are indicated as a tendency as compared to the Ni cation. On charging, the behavior of Co is in line with the behavior of Ni, the edges shift to higher energies in agreement with the oxidation of the Co cation (see Fig. 12 and S5†), the equatorial bond distances contract by about 5 pm and the apical distance increases by about 25 pm. However, on discharging by 60 mA h g^{-1}, only the equatorial site expands to a bond distance close to what has been observed for the original sample, and the apical bond distances remain high at around 260 pm (see Table 2). The edge position becomes similar to before charging but indicates a slightly higher oxidation state than in the original sample. We hypothesize that this could be interpreted by the formation of Co^{3+} in an intermediate $e_g^4b_{2g}^1a_{1g}^1$ (for d-orbital splitting in D_{4h} symmetry) spin state, which can be well stabilized in a more square-planar-related coordination. The large distance of the apical site indicates that the coordination around the Co-cation is more similar to a T′ RP-type structure as observed for Nd_2CuO_4 with oxide ions occupying the equatorial and interstitial anion sites. On discharging the sample further to 180 mA h g^{-1}, the edge of Co shifts to a value which is 1.2 eV lower than the sample before charging. This change of oxidation state is additionally accompanied by an increase of the equatorial anion distance to 196 pm (again in conceptual agreement with increased lattice parameters a/b derived from diffraction analysis) and the apical bond distance reduces to 230 pm length. This indicates that oxidation states around or even lower than +2 might be possible on electrochemical reduction, which has been observed in chemical reduction of perovskite-related cobaltates before.[49,50]

Table 2 Co–O bond distances of $La_2Ni_{0.75}Co_{0.25}O_{4.08}$ under different charging/discharging conditions. Errors are in the order of ±0.06–0.11 for the equatorial (eq.) and of ±0.10–0.18 for the apical (ap.) bond distances. Therefore, the determined trend is more robust than the absolute values. The errors are higher than for the Ni–O distances and could not be determined reliably. Therefore, the determined trend is more robust than the absolute values

Sample	Co–O eq. bond (pm)	Co–O ap. bond (pm)
Cathode composite	191	219
Charged up to 50 mA h g^{-1}	189	215
Charged up to 90 mA h g^{-1}	191	247
Charged up to 110 mA h g^{-1}	189	236
Charged up to 130 mA h g^{-1}	186	251
Discharged up to 20 mA h g^{-1}	188	250
Discharged up to 40 mA h g^{-1}	189	259
Discharged up to 60 mA h g^{-1}	190	261
Discharged up to 180 mA h g^{-1}	196	231

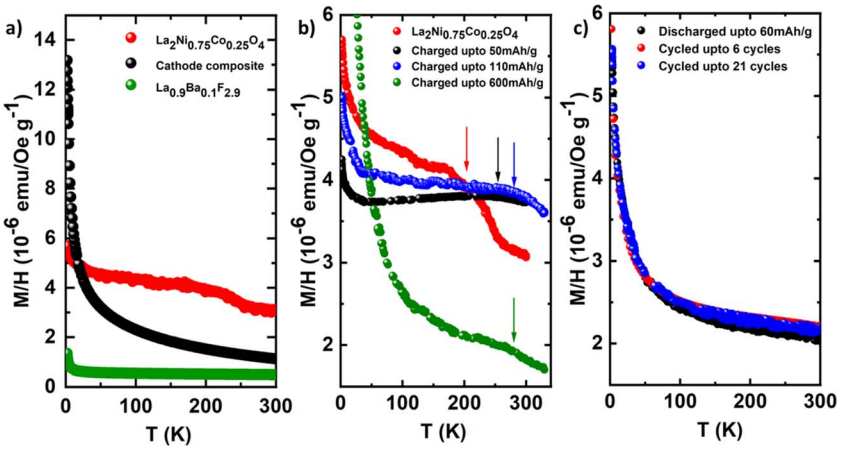

Fig. 13 Magnetization as a function of temperature and external magnetic field measured in (a) pristine $La_2Ni_{0.75}Co_{0.25}O_{4.08}$, (b) cathode composite of $La_2Ni_{0.75}Co_{0.25}O_{4.08}$ and different charging and (c) cycled state of $La_2Ni_{0.75}Co_{0.25}O_{4.08}$.

Thus, the XAS analysis reveals that doping of La_2NiO_4 with Co induces a complex structural fluorination chemistry and that the fluorine incorporation, though occurring at decent coulombic efficiency might induce differences in the local surroundings of the different transition metal cations, which have an impact on the electrochemical properties.

3.4 Influence of charging/discharging on magnetic properties of $La_2Ni_{0.75}Co_{0.25}O_{4.08}$

To further characterize the $La_2Ni_{0.75}Co_{0.25}O_{4.08}$ compound, magnetic measurements were performed on the pristine, cathode composite, charged/discharged cells and cycled cells as shown in Fig. 13.

The magnetic susceptibility of pure $La_2NiO_{4+\delta}$, due to the flexibility of oxygen content δ, has been studied in a vast amount of literature with different results.[51–53]. Stoichiometric La_2NiO_4 is an orthorhombic (*Bmab*), brown, semiconducting, and antiferromagnetically ordered material below room temperature. Furthermore, it also transforms to a tetragonal modification with space group *I*4/*mmm* at temperatures above 700 K and shows an orthorhombic-to-orthorhombic transition at low temperatures, *i.e.* below 80 K.[54]

In contrast, oxidized $La_2NiO_{4+\delta}$ ($0 < \delta < 0.25$) is a black material, which lacks 3D long-range order at any temperature below 300 K.[54] Finally, with $La_2NiO_{4.25}$ *i.e.* $La_8Ni_4O_{17}$ clear oxygen ordering was observed with *Fmmm* at room temperature, but still no magnetic Bragg peaks were observed extending up to $\delta = 0.34$.[55]

$La_2CoO_{4.25}$ was shown to order antiferromagnetically at 36 K with both oxygen and charge ordering *via* neutron diffraction.[56] In contrast, La_2CoO_4 undergoes a Néel-type order at 275 K and a structural transition at 135 K to the tetragonal phase.[57] For the substituted $La_2Ni_{0.75}Co_{0.25}O_{4.08}$ composite, no sharp transitions in susceptibility were expected due to the observations on the two parent compounds. As shown by the red curve in Fig. 13a, the susceptibility *versus* temperature in an applied field of 1 T shows a broad maximum in the susceptibility around 200 K, with the onset of an increase around 250 K. Since $La_2Ni_{0.75}Co_{0.25}O_{4.08}$ (black curve) already has an increased oxygen content no clear magnetic transition is expected and the origin of this maximum originates from the exchange interaction in low dimensional quantum magnets as this typical 2D Heisenberg magnet. The base sample for the reaction is a mixture of the $La_2Ni_{0.75}Co_{0.25}O_{4.08}$ composite with $La_{0.9}Ba_{0.1}F_{2.9}$, which shows in the entire temperature range a paramagnetic contribution due to the nonmagnetic sample signal mixed with the sample holder (see Fig. 13a). The charged samples also contain diamagnetic graphene nanoparticles leading to a largely changed signal shown in Fig. 13a, where no maximum is apparent. Thus, for the measurements, it was tried to extract solely the $La_2Ni_{0.75}Co_{0.25}O_{4.08}F_y$ part from the pellet. Hence, we plot the effective susceptibility in emu/Oe g^{-1} and note that the precise mass ratios of each sample might vary slightly, due to the different amounts of contamination with the base mixture as described earlier by Vasala *et al.*[58]

For the $M(H)$ curves, a subtle hysteresis dominated by a Brillouin function with a very low moment of 0.002 μ_B for the pure $La_2Ni_{0.75}Co_{0.25}O_{4.08}$ was observed (not shown). Given the impossibility of dividing by the real molar masses due to a mixture in the fluorinated compounds, the $M(H)$ curves in detail were not analysed but found in all a similar shape and coercivity.

In Fig. 13b, the effect of fluorination on the susceptibility of the cells charged at 50, 110 and 600 mA h g^{-1} is shown. This electrochemical fluorination of $La_2Ni_{0.75}Co_{0.25}O_{4.08}$ leads to changes in the susceptibility, without the appearance of long-range order (similar to increasing oxygen intercalation from $0.08 < \delta < 0.34$). It was found that with increasing charge the maximum shifts towards higher temperatures (highlighted by an arrow). This effect is in principle in agreement with what has been observed for oxygen intercalation, which effectively happens when increasing delta in $La_2NiO_{4+\delta}$ as we are separating the layers producing more 2D physics. Likely the Ni–O–Ni buckling decreases, which increases in-plane J_s. For the maximum charge saturation is reached and instead disorder increased producing a less pronounced maximum. Finally, in

Fig. 13c, the effect of cycling on the susceptibility is shown. No major effect on the susceptibility was observed besides a subtly varying signal strength due to the described varying contents of phases from repeated cycling. Notably however upon discharging or defluorination, we do not recover the susceptibility of pure $La_2Ni_{0.75}Co_{0.25}O_{4.08}$ likely due to a larger amount of disorder, which is also in agreement with the observations made in powder diffraction as well as the evaluation of XAS data.

4 Conclusions

In this study, we have demonstrated the first multi-transition element containing Ruddlesden–Popper-type $La_2Ni_{0.75}Co_{0.25}O_{4.08}$ as a cathode material for all-solid-state FIBs. Increasing the elemental complexity at the octahedrally coordinated transition metal site has changed the electrochemical behaviour of the material and makes it different from the parent compounds: La_2CoO_4 and La_2NiO_4. Detailed structural analysis *via* XRD has shown the successful insertion and removal of fluoride ions from the vacant anion rock salt interlayers of $La_2Ni_{0.75}Co_{0.25}O_{4.08}$, confirming the reversible fluorination/defluorination under maintenance of the lattice. XAS measurements have clearly shown the change in the oxidation state of Ni and Co upon electrochemical fluorination and the coordination environment around the transition metals such as contraction of the octahedron. Thus, the doping of La_2NiO_4 with cobalt has induced more complex structural fluorination chemistry with differences in the local surroundings, impacting the electrochemical properties. Regarding the interactions with the carbon matrix, Co also seems to be a strong player for introducing side reactions, though it also leads to more stable cycling closer to the maximum theoretical capacity compared to pure nickelates.

At the moment, the full capacity of ~140 mA h g^{-1} of RP-type materials has not been accessed in extended cycling experiments. Also, mixed cation compositions do not change this in a drastic manner, since the carbon additives appear to be too unstable. However, by minimizing the interactions with the carbon matrix independently (*e.g.*, by choosing different geometries or different chemical approaches for the additives), mixed cation compounds might indeed help to obtain improved properties for a cathode material. Further, the anode chemistries would also have to be optimized in a similar way,[30] to obtain high voltage batteries with properties more similar to current LIB systems.[1]

Author contributions

V. V.: writing the manuscript, executing the synthesis of the precursors, preparation of electrochemical cells and samples for further characterization measurements such as diffraction experiments, SEM-EDAX, electrochemical characterization, XAS measurement, magnetic measurements, and analysis of XRD, XAS and GCPL data including plotting of all the data. A. I. W.: guided the synthesis part in order to get a phase pure compound. P. P.: performed the magnetic measurements, plotted and analyzed the data. S. V. and R. S.: performed X-ray absorption spectroscopy with guidance from P. G. and M. B. S. V.: analyzed EXAFS data using X-ray Larch software. O. C.: designed the study and supervised the project. All authors read the final version of the manuscript and contributed to it by writing, corrections and/or suggestions.

Conflicts of interest

The authors declare no conflicts of interest.

Acknowledgements

This work was funded by the German Research Foundation within the Emmy Noether program (Grant CL 551/2-1). AMICA, Uni Stuttgart is acknowledged for providing access to the SEM device.

References

1 J.-K. Park, *Principles and Applications of Lithium Secondary Batteries*, John Wiley & Sons, 2012.
2 M. Akhilash, P. S. Salini, K. Jalaja, B. John and T. D. Mercy, Synthesis of $Li_{1.5}Ni_{0.25}Mn_{0.75}O_{2.5}$ cathode material via carbonate co-precipitation method and its electrochemical properties, *Inorg. Chem. Commun.*, 2021, **126**, 108434.
3 M. Akhilash, P. S. Salini, B. John and T. D. Mercy, A journey through layered cathode materials for lithium ion cells - From lithium cobalt oxide to lithium-rich transition metal oxides, *J. Alloys Compd.*, 2021, **869**, 159239.
4 S. Chen, T. He, Y. Su, Y. Lu, L. Bao, L. Chen, Q. Zhang, J. Wang, R. Chen and F. Wu, Ni-Rich $LiNi_{0.8}Co_{0.1}Mn_{0.1}O_2$ Oxide Coated by Dual-Conductive Layers as High Performance Cathode Material for Lithium-Ion Batteries, *ACS Appl. Mater. Interfaces*, 2017, **9**(35), 29732–29743.
5 J. Liu and A. Manthiram, Understanding the Improved Electrochemical Performances of Fe-Substituted 5 V Spinel Cathode $LiMn_{1.5}Ni_{0.5}O_4$, *J. Phys. Chem. C*, 2009, **113**(33), 15073–15079.
6 X. He, S. Su, B. Zhang, Z. Xiao, Z. Zhang and X. Ou, Alleviating the anisotropic microstructural change and boosting the lithium ions diffusion by grain orientation regulation for Ni-rich cathode materials, *J. Energy Chem.*, 2024, **88**, 213–222.
7 *List of Mineral Species*, **https://www.mindat.org/min-1576.html**.
8 F. Gschwind, H. Euchner and G. Rodriguez-Garcia, Chloride Ion Battery Review: Theoretical Calculations, State of the Art, Safety, Toxicity, and an Outlook towards Future Developments, *Eur. J. Inorg. Chem.*, 2017, **2017**(21), 2784–2799.
9 M. Anji Reddy and M. Fichtner, Batteries based on fluoride shuttle, *J. Mater. Chem.*, 2011, **21**(43), 17059–17062.
10 K. Wissel, S. Dasgupta, A. Benes, R. Schoch, M. Bauer, R. Witte, A. D. Fortes, E. Erdem, J. Rohrer and O. Clemens, Developing intercalation based anode materials for fluoride-ion batteries: topochemical reduction of

$Sr_2TiO_3F_2$via a hydride based defluorination process, *J. Mater. Chem. A*, 2018, **6**(44), 22013–22026.

11 F. Gschwind, Z. Zao-Karger and M. Fichtner, A fluoride-doped PEG matrix as an electrolyte for anion transportation in a room-temperature fluoride ion battery, *J. Mater. Chem. A*, 2014, **2**(5), 1214–1218.

12 Y. Yu, M. Lei, D. Li and C. Li, Near-Room-Temperature Quasi-Solid-State F-Ion Batteries with High Conversion Reversibility Based on Layered Structured Electrolyte, *Adv. Energy Mater.*, 2023, **13**(12), 2203168.

13 Y. Yu, M. Lei and C. Li, Room-temperature reversible F-ion batteries based on sulfone electrolytes with a mild anion acceptor additive, *Mater. Horiz.*, 2024, **11**(2), 480–489.

14 Y. Yu, A. Lin, M. Lei, C. Lai, C. Wu, Y.-Y. Sun and C. Li, High-Capacity and Long-Cycling F-Ion Pouch Cells Enabled by Green Electrolytes, *ACS Energy Lett.*, 2024, 1008–1016.

15 K. Nakayama, R. Ishikawa, T. Tojigamori, H. Miki, H. Iba, N. Shibata and Y. Ikuhara, Fluoride-ion conversion alloy for fluoride-ion batteries, *J. Mater. Chem. A*, 2022, **10**(7), 3743–3749.

16 D. T. Thieu, M. Hammad, H. Bhatia, T. Diemant, V. S. K. Chakravadhanula, R. J. Behm, C. Kubel and M. Fichtner, CuF_2 as Reversible Cathode for Fluoride Ion Batteries, *Adv. Funct. Mater.*, 2017, **27**(31), 1701051.

17 M. A. Nowroozi, I. Mohammad, P. Molaiyan, K. Wissel, A. R. Munnangi and O. Clemens, Fluoride ion batteries - past, present, and future, *J. Mater. Chem. A*, 2021, **9**(10), 5980–6012.

18 L. Zhang, M. A. Reddy, P. Gao, T. Diemant, R. Jürgen Behm and M. Fichtner, Study of all solid-state rechargeable fluoride ion batteries based on thin-film electrolyte, *J. Solid State Electrochem.*, 2017, **21**, 1243–1251.

19 T. Yoshinari, D. T. Zhang, K. Yamamoto, Y. Kitaguchi, A. Ochi, K. Nakanishi, H. Miki, S. Nakanishi, H. Iba, T. Uchiyama, T. Watanabe, T. Matsunaga, K. Amezawa and Y. Uchimoto, Kinetic analysis and alloy designs for metal/metal fluorides toward high rate capability for all-solid-state fluoride-ion batteries, *J. Mater. Chem. A*, 2021, **9**(11), 7018–7024.

20 D. T. Zhang, K. Yamamoto, A. Ochi, Y. C. Wang, T. Yoshinari, K. Nakanishi, H. Nakano, H. Miki, S. Nakanishi, H. Iba, T. Uchiyama, T. Watanabe, K. Amezawa and Y. Uchimoto, Understanding the reaction mechanism and performances of 3d transition metal cathodes for all-solid-state fluoride ion batteries, *J. Mater. Chem. A*, 2021, **9**(1), 406–412.

21 J. Haruyama, K. I. Okazaki, Y. Morita, H. Nakamoto, E. Matsubara, T. Ikeshoji and M. Otani, Two-Phase Reaction Mechanism for Fluorination and Defluorination in Fluoride-Shuttle Batteries: A First-Principles Study, *ACS Appl. Mater. Interfaces*, 2020, **12**(1), 428–435.

22 L. Zhang, M. A. Reddy and M. Fichtner, Development of tysonite-type fluoride conducting thin film electrolytes for fluoride ion batteries, *Solid State Ionics*, 2015, **272**, 39–44.

23 M. A. Nowroozi, S. Ivlev, J. Rohrer and O. Clemens, La_2CoO_4: a new intercalation based cathode material for fluoride ion batteries with improved cycling stability, *J. Mater. Chem. A*, 2018, **6**(11), 4658–4669.

24 M. A. Nowroozi, K. Wissel, M. Donzelli, N. Hosseinpourkahvaz, S. Plana-Ruiz, U. Kolb, R. Schoch, M. Bauer, A. M. Malik, J. Rohrer, S. Ivlev, F. Kraus and O. Clemens, High cycle life all-solid-state fluoride ion battery with La_2NiO_{4+d} high voltage cathode, *Commun. Mater.*, 2020, **1**(1), 27.

25 M. A. Nowroozi, K. Wissel, J. Rohrer, A. R. Munnangi and O. Clemens, LaSrMnO4: Reversible Electrochemical Intercalation of Fluoride Ions in the Context of Fluoride Ion Batteries, *Chem. Mater.*, 2017, **29**(8), 3441–3453.

26 K. Wissel, R. Schoch, T. Vogel, M. Donzelli, G. Matveeva, U. Kolb, M. Bauer, P. R. Slater and O. Clemens, Electrochemical Reduction and Oxidation of Ruddlesden-Popper-Type $La_2NiO_3F_2$ within Fluoride-Ion Batteries, *Chem. Mater.*, 2021, **33**(2), 499–512.

27 O. Clemens, M. Kuhn and R. Haberkorn, Synthesis and characterization of the $La_{1-x}Sr_xFeO_{3-\delta}$ system and the fluorinated phases $La_{1-x}Sr_xFeO_{3-x}F_x$, *J. Solid State Chem.*, 2011, **184**(11), 2870–2876.

28 E. E. McCabe and C. Greaves, Fluorine insertion reactions into pre-formed metal oxides, *J. Fluorine Chem.*, 2007, **128**(4), 448–458.

29 T. Sivakumar and J. B. Wiley, Topotactic route for new layered perovskite oxides containing fluorine: Ln1.2Sr1.8Mn2O7F2 (Ln=Pr, Nd, Sm, Eu, and Gd), *Mater. Res. Bull.*, 2009, **44**(1), 74–77.

30 M. A. Nowroozi, On the Development of Intercalation-Based Cathode Materials for All-Solid-State Fluoride Ion Batteries, TUprints:11523, 2020.

31 Y. Wang, K. Yamamoto, Y. Tsujimoto, T. Matsunaga, D. Zhang, Z. Cao, K. Nakanishi, T. Uchiyama, T. Watanabe, T. Takami, H. Miki, H. Iba, K. Maeda, H. Kageyama and Y. Uchimoto, Anion Substitution at Apical Sites of Ruddlesden–Popper-type Cathodes toward High Power Density for All-Solid-State Fluoride-Ion Batteries, *Chem. Mater.*, 2022, **34**(2), 609–616.

32 K. Yamamoto, Development of Electrode Materials Based on Design Guideline of Electronic Structure Obtained by Synchrotron Radiation X-ray Analyses, *Electrochemistry*, 2023, **91**(10), 102004.

33 Y. C. Wang, K. Yamamoto, Y. Tsujimoto, T. Matsunaga, D. T. Zhang, Z. L. Cao, K. Nakanishi, T. Uchiyama, T. Watanabe, T. Takami, H. Miki, H. Iba, K. Maeda, H. Kageyama and Y. Uchimoto, Anion Substitution at Apical Sites of Ruddlesden-Popper-type Cathodes toward High Power Density for All-Solid-State Fluoride-Ion Batteries, *Chem. Mater.*, 2022, **34**(2), 609–616.

34 J. B. Goodenough and K. S. Park, The Li-ion rechargeable battery: A Perspective, *J. Am. Chem. Soc.*, 2013, **135**(4), 1167–1176.

35 R. Bonne and J. Schoonman, The ionic conductivity of beta lead fluoride, *J. Electrochem. Soc.*, 1977, **124**(1), 28.

36 *Larch: Data Analysis Tools for X-Ray Spectroscopy*, **https://xraypy.github.io/xraylarch/index.html**.

37 A. Grenier, A. G. Porras-Gutierrez, M. Body, C. Legein, F. Chretien, E. Raymundo-Pinero, M. Dolle, H. Groult and D. Dambournet, Solid Fluoride Electrolytes and Their

Composite with Carbon: Issues and Challenges for Rechargeable Solid State Fluoride-Ion Batteries, *J. Phys. Chem. C*, 2017, **121**(45), 24962–24970.

38 M. A. Nowroozi and O. Clemens, Insights on the Behavior of Conversion-Based Anode Materials for Fluoride Ion Batteries by Testing against an Intercalation-Based Reference Cathode, *ACS Appl. Energy Mater.*, 2018, **1**(11), 6626–6637.

39 M. A. Nowroozi, B. de Laune and O. Clemens, Reversible Electrochemical Intercalation and Deintercalation of Fluoride Ions into Host Lattices with Schafarzikite-Type Structure, *ChemistryOpen*, 2018, **7**(8), 617–623.

40 N. J. Dudney, W. C. West and J. Nanda, *Handbook of solid state batteries*, World Scientific, 2015, vol. 6.

41 K. Wissel, Topochemical fluorination and defluorination in the context of fluoride-ion batteries and tuning of magnetic properties, TUprints:13383, 2020.

42 K. Wissel, A. M. Malik, S. Vasala, S. Plana-Ruiz, U. Kolb, P. R. Slater, I. da Silva, L. Alff, J. Rohrer and O. Clemens, Topochemical reduction of $La_2NiO_3F_2$: the first Ni-based Ruddlesden–Popper n= 1 T′-type structure and the impact of reduction on magnetic ordering, *Chem. Mater.*, 2020, **32**(7), 3160–3179.

43 K. Wissel, F. Bernardini, H. Oh, S. Vasala, R. Schoch, B. Blaschkowski, P. Glatzel, M. Bauer, O. Clemens and A. Cano, Single-Layer T'; Nickelates: Synthesis of the La and Pr Members and Electronic Properties across the Rare-Earth Series, *Chem. Mater.*, 2022, **34**(16), 7201–7209.

44 H. Touhara, J. Inahara, T. Mizuno, Y. Yokoyama, S. Okanao, K. Yanagiuch, I. Mukopadhyay, S. Kawasaki, F. Okino, H. Shirai, W. H. Xu, T. Kyotani and A. Tomita, Property control of new forms of carbon materials by fluorination, *J. Fluorine Chem.*, 2002, **114**(2), 181–188.

45 H. Touhara and F. Okino, Property control of carbon materials by fluorination, *Carbon*, 2000, **38**(2), 241–267.

46 Z. Tu, P. Nath, Y. Lu, M. D. Tikekar and L. A. Archer, Nanostructured electrolytes for stable lithium electrodeposition in secondary batteries, *Acc. Chem. Res.*, 2015, **48**(11), 2947–2956.

47 Y. J. Zhang, W. Wang, H. Tang, W. Q. Bai, X. Ge, X. L. Wang, C. D. Gu and J. P. Tu, An ex-situ nitridation route to synthesize Li_3N-modified Li anodes for lithium secondary batteries, *J. Power Sources*, 2015, **277**, 304–311.

48 R. J. Woolley, B. N. Illy, M. P. Ryan and S. J. Skinner, In situ determination of the nickel oxidation state in $La_2NiO_{4+\delta}$ and $La_4Ni_3O_{10-\delta}$ using X-ray absorption near-edge structure, *J. Mater. Chem.*, 2011, **21**(46), 18592–18596.

49 A. I. Waidha, L. Ni, J. Ali, M. Lepple, M. Donzelli, S. Dasgupta, S. Wollstadt, L. Alff, U. Kramm and O. Clemens, Synthesis of bifunctional $BaFe_{1-x}Co_xO_{3-y-\delta}(OH)_y$ catalysts for the oxygen reduction reaction and oxygen evolution reaction, *J. Mater. Chem. A*, 2020, **8**(2), 616–625.

50 A. I. Waidha, Developing nebulized spray pyrolysis as a synthesis route for energy materials: Composite electrolytes and mixed electron-proton-conductors, TUprints:20773, 2022.

51 R. R. Schartman and J. M. Honig, Magnetic susceptibility investigations of the $La_2NiO_{4+\delta}$ system, *Mater. Res. Bull.*, 1989, **24**(6), 671–679.

52 D. J. Buttrey, J. M. Honig and C. N. R. Rao, Magnetic properties of quasi-two-dimensional La_2NiO_4, *J. Solid State Chem.*, 1986, **64**(3), 287–295.

53 N. J. Poirot, C. Allançon, P. Odier, P. Simon, J. M. Bassat and J. P. Loup, Magnetic Properties of $La_2NiO_{4.16}$and $La_{2-x}Pr_xNiO_{4+\delta}$, *J. Solid State Chem.*, 1998, **138**(2), 260–266.

54 R. Sáez-Puche, F. Fernández, J. L. Martínez and J. Rodríguez-Carvajal, Neutron diffraction study on the orthorhombic form of La_2NiO_4, *J. Less-Common Met.*, 1989, **149**, 357–361.

55 A. Aguadero, J. Alonso, M. Martínez-Lope, M. Fernandez-Diaz, M. Escudero and L. Daza, In situ high temperature neutron powder diffraction study of oxygen-rich $La_2NiO_{4+\delta}$ in air: correlation with the electrical behaviour, *J. Mater. Chem.*, 2006, **16**(33), 3402–3408.

56 R. De Barros, M. Ceretti, W. Schmidt, V. Y. Pomjakushin and W. Paulus, Growth and Oxygen Stoichiometry Control of High-Quality $La_2CoO_{4+\delta}$ Single Crystals ($\delta = 0.25$), *Cryst. Growth Des.*, 2022, **22**(9), 5542–5551.

57 K. Yamada, M. Matsuda, Y. Endoh, B. Keimer, R. J. Birgeneau, S. Onodera, J. Mizusaki, T. Matsuura and G. Shirane, Successive antiferromagnetic phase transitions in single-crystal La_2CoO_4, *Phys. Rev. B: Condens. Matter Mater. Phys.*, 1989, **39**(4), 2336–2343.

58 S. Vasala, A. Jakob, K. Wissel, A. I. Waidha, L. Alff and O. Clemens, Reversible Tuning of Magnetization in a Ferromagnetic Ruddlesden-Popper-Type Manganite by Electrochemical Fluoride-Ion Intercalation, *Adv. Electron. Mater.*, 2020, **6**(2), 1900974.

